The Solution Structure of BMPR-IA Reveals a Local Disorder-to-Order Transition upon BMP-2 Binding[†,‡]

Jochen Klages,[§,||] Alexander Kotzsch,[||,⊥] Murray Coles,[@] Walter Sebald,[#] Joachim Nickel,[#] Thomas Müller,*[,⊥] and Horst Kessler*[,§]

Center of Integrated Protein Science (CIPSM) at the Technische Universität München, Lichtenbergstrasse 4, D-85747 Garching, Germany, Lehrstuhl für Botanik I-Molekulare Pflanzenphysiologie and Biophysik, Julius-von-Sachs-Institut für Biowissenschaften (Biozentrum) der Universität Würzburg, Julius-von-Sachs-Platz 2, D-97082 Würzburg, Germany, Department of Protein Evolution, Max-Planck-Institute for Developmental Biology, Spemannstrasse 35, D-72076 Tübingen, Germany, and Lehrstuhl für Physiologische Chemie II, Theodor-Boveri-Institut für Biowissenschaften (Biozentrum) der Universität Würzburg, Am Hubland, D-97074 Würzburg, Germany

Received June 5, 2008; Revised Manuscript Received September 12, 2008

ABSTRACT: The structure of the extracellular domain of BMP receptor IA was determined in solution by NMR spectroscopy and compared to its structure when bound to its ligand BMP-2. While most parts of the secondary structure are highly conserved between the bound and unbound forms, large conformational rearrangements can be observed in the $\beta4\beta5$ loop of BMPR-IA, which is in contact with BMP-2 and harbors the main binding determinants for the BMPR-IA−BMP-2 interaction. In its unbound form, helix α1 in BMPR-IA, which is in the center of the binding epitope for BMP-2, is missing. Since BMP-2 also shows conformational changes in the type I receptor epitope upon binding to BMPR-IA, both binding partners pass through an induced fit mechanism to adapt their binding interfaces to a given interaction surface. The inherent flexibility of both partners possibly explains the promiscuous ligand−receptor interaction observed in the BMP protein superfamily.

Bone morphogenetic proteins (BMPs)[1] belong to the superfamily of transforming growth factors-β (TGF-β). This superfamily consists of more than 40 secreted signaling proteins like TGF-βs, BMPs, growth and differentiation factors (GDFs), activines, inhibines, muellerian inhibiting substance (MIS), and glial-derived neurotrophic growth factor (GDNF) (*1*). Comprising more than 15 members, BMPs and GDFs form the largest subgroup within this superfamily. The function of BMPs is highly diverse, acting on many different cell types, such as epithelial, mesenchymal, and neuronal cells, thereby regulating proliferation, differentiation, chemotaxis, and apoptosis of these cells (*2*). BMPs exert a central function in embryonic development, from the very early establishment of the dorsal/ventral body axis to the later formation of organs, e.g., kidney, eye, limb, amnion, heart, and testis (*3*). Because of their omnipresent character, failure as well as dysregulation of BMP signaling leads to severe diseases, e.g., skeletal abnormalities or metabolic disorders (*4*).

Signaling is achieved via single-span transmembrane serine/threonine-kinase receptors, which can be subdivided into two types on the basis of their structural and functional properties (*1*). In a sequential binding mechanism the ligand assembles two type I and two type II receptors into a heterotetrameric receptor complex. In the case of BMP-2, the ligand BMP-2 binds first with high affinity to BMP type I receptor BMPR-IA or BMPR-IB forming a binary complex. Subsequently, low-affinity BMP type II receptors, e.g., BMPR-II, ActR-II, and ActR-IIB, are recruited into the complex. The formation of the complex of BMP-2 and type I and type II receptors results in intracellular phosphorylation of the type I receptor by the constitutively active type II receptor kinase and leads to activation of the SMAD proteins. The activated SMAD proteins then translocate to the nucleus and regulate gene transcription of BMP-responsive genes.

A hallmark of the BMP superfamily is its highly promiscuous ligand−receptor interaction. BMP-2 binds to the two

[†] This project was supported by the Deutsche Forschungsgemeinschaft (DFG), Grants MU1095/1-1 and KE147/40-1.

[‡] The coordinates of 20 calculated structures of BMPR-IA have been deposited with the Protein Data Bank (entry 2k3g). Chemical shift assignments and relaxation data have been deposited with the BioMagResBank (entry 15956).

* To whom correspondence should be addressed. H.K.: e-mail, horst.kessler@ch.tum.de; phone, +49 89-289 13300; fax, +49 89-289 13210. T.D.M.: e-mail, mueller@botanik.uni-wuerzburg.de; phone, +49 931 888 6146; fax, +49 931 888 6158.

[§] Center of Integrated Protein Science (CIPS) at the Technische Universität München.

[||] These authors contributed equally to this work.

[⊥] Julius-von-Sachs-Institut für Biowissenschaften (Biozentrum) der Universität Würzburg.

[@] Max-Planck-Institute for Developmental Biology.

[#] Theodor-Boveri-Institut für Biowissenschaften (Biozentrum) der Universität Würzburg.

[1] Abbreviations: BMP-2, bone morphogenetic protein 2; GDF-5, growth and differentiation factor 5; BMPR-IA, BMP receptor type IA; BMPR-IB, BMP receptor type IB; ActR-II, activin receptor type II; SMAD, small mothers against decapentaplegic; ECD, extracellular domain; ITC, isothermal titration calorimetry; CD, circular dichroism; NMR, nuclear magnetic resonance; COSY, correlation spectroscopy; TOCSY, total correlation spectroscopy; NOESY, nuclear Overhauser effect spectroscopy; HSQC, heteronuclear single-quantum correlation; S^2, squared order parameter; $\langle S^2 \rangle$, average squared order parameter; TFE, trifluoroethanol.

10.1021/bi801059j CCC: $40.75
Published on Web 10/21/2008

type I receptors, BMPR-IA and BMPR-IB, with almost identical affinity. In addition, three different type II receptors, BMPR-II and activin type II receptors ActR-II and ActR-IIB, can be recruited into the complex alike, leading to similar SMAD activation (*5*). During the past years, several structures of BMPs bound to the extracellular domains (ECD) of type I and type II receptors have been published, yielding a first glimpse into how binding affinity is generated and how promiscuous binding to different type I and type II receptors might be achieved (*6*−*11*). To date, three crystal structures of BMPR-IA_{ECD} bound to BMP-2 have been determined, showing that irrespective of crystallization conditions the binding and structure of BMPR-IA_{ECD} are basically identical in all three cases (*6, 8, 10*). However, in contrast to the type II receptors, no structures of the BMP type I receptors in their unbound state have been determined. A preliminary NMR investigation of BMRP-IA_{ECD} suggested that structures of BMPR-IA in the bound and unbound state might differ (*12*). However, the resolution of the structure data was low, and the coordinates were never released.

Since structures of free BMP-2 and BMP-2 bound to BMPR-IA_{ECD} show that a central element of BMP-2, the prehelix loop, takes part in an induced fit mechanism, it would be highly interesting to determine whether this prehelix loop adapts to an already preformed surface on BMPR-IA or whether both interaction partners simultaneously form their interaction surfaces upon complex formation. The fact that maintenance of the scaffold of BMPR-IA is essential for its function was recently shown in another study. Several mutations in the extracellular domain of BMPR-IA found in the disease juvenile polyposis syndrome (JPS) lead to unfolding of BMPR-IA, thereby causing a loss of binding to BMPs (*9*). Thus, determining whether, where, and to what extent the extracellular domain of BMPR-IA exhibits flexibility is an important prerequisite for understanding recognition and promiscuous binding in the BMP system.

Here we report the high-resolution NMR structure of BMPR-IA_{ECD} in solution, revealing that a large part of the ligand-binding epitope is unfolded and flexible before formation of the complex. The binding $\beta4\beta5$ loop of BMPR-IA passes through a structural rearrangement upon BMP-2 binding. This is in contrast to the mechanism observed for the type II receptors, where the majority of the ligand-binding epitope is already preformed and changes are found only at the periphery of the interface. Although a preformed interface is often assumed as a requirement for high-affinity binding, the flexible interfaces of the ligand BMP-2 as well as of its receptor BMPR-IA might well explain the possible coexistence of high-affinity binding and promiscuity in BMP−type I receptor interaction.

MATERIALS AND METHODS

Protein Expression and Purification. The extracellular domain (ECD) of human BMPR-IA (amino acids 1−129 of the mature part, SWISSPROT entry P36894) and BMP-2 were expressed as described previously (*13, 14*). A truncated version of BMPR-IA lacking most of the flexible N-terminus (amino acids 29−129 of the mature part) was cloned by engineering a PreScission protease site (exchanges E22L, N23E, G24V, V25L, T26F, L27Q, and A28G) in front of residue Pro29 since the N-terminal sequence is needed for proper folding of the thioredoxin fusion protein. NMR analysis of this N-terminally truncated variant BMPR-IA_{SF} shows a significantly improved two-dimensional (2D) HSQC spectrum; most of the peaks indicative of residues in highly flexible regions present in the spectrum of BMPR-IA_{ECD} were absent (Figure 1 of the Supporting Information).

Uniform isotopic labeling of the receptor ectodomains was achieved by protein expression in *Escherichia coli* BL21(DE3) grown in M9 minimal medium according to published protocols (*15*). For incorporation of ^{15}N, the medium was supplemented with 0.5 g/L $^{15}NH_4Cl$ (98%, CK Gas Products Ltd.), and 7.5 g/L glucose was used to facilitate high-level protein expression. For double labeling with ^{15}N and ^{13}C, the medium was supplemented with 0.5 mg/L $^{15}NH_4Cl$ and 4 g/L [U-$^{13}C_6$]glucose (99%, CK Gas Products Ltd.).

For purification of BMPR-IA_{ECD} or BMPR-IA_{SF}, transformed *E. coli* cells were grown overnight after induction at 20 °C, and cells were then harvested and disrupted by sonication. The supernatant was subjected to Ni^{2+}-NTA affinity chromatography (Qiagen). Cleavage of the BMPR-IA_{ECD}/BMPR-IA_{SF}−thioredoxin fusion proteins was achieved with thrombin. The cleavage products were separated by anion exchange chromatography using EMD-TMAE material (Merck). For the generation of the shortened version BMPR-IA_{SF}, the BMPR-IA_{SF} precursor was additionally processed using PreScission protease, which cleaves behind Gln27 leaving Gly28 as the first N-terminal residue of BMPR-IA_{SF}. Active and monomeric BMPR-IA_{ECD}/BMPR-IA_{SF} proteins were obtained by employing an affinity chromatography using a resin with immobilized BMP-2. The average protein yield for ^{15}N-labeled or ^{15}N- and ^{13}C-labeled BMPR-IA_{ECD}/BMPR-IA_{SF} was ∼0.6 mg/L of minimal medium.

The purity and homogeneity of all proteins were verified by SDS−PAGE, ESI-FT-ICR mass spectrometry, and RP-HPLC. To check for protein activity, binding affinities of BMP-2 and BMPR-IA_{SF} were determined by the surface plasmon resonance (SPR) method as described in refs *10* and *16* and compared to values reported in the literature (*8*).

Isothermal Titration Calorimetry. The thermodynamic parameters for formation of the binary complex of BMP-2 and BMPR-IA_{ECD} were determined using a VP-ITC microcalorimeter (MicroCal Inc., Northampton, MA). All solutions used for titration experiments were degassed at 18 °C for 10 min. BMP-2 and BMPR-IA_{ECD} were dissolved in 10 mM HEPES (pH 7.4) and 500 mM NaCl. For the ITC experiment, a 50.0 μM BMPR-IA_{ECD} solution was added stepwise to a 1.8 μM BMP-2 solution. After the first injection of 5 μL of the BMPR-IA_{ECD} solution (1 μL/s) and a 360 s equilibration period, a titration was performed by 14 injections (10 μL each, 1 μL/s), with a stirring rate of 300 rpm, and a delay time of 300 s between the injections. Data analysis was carried out using MicroCal Origin (version 7.0). Data points were fitted using a one-site binding model.

NMR Structural and Dynamical Analysis of BMPR-IA_{SF}. NMR analysis was performed using a sample of 0.5 mM [^{15}N,^{13}C]BMPR-IA_{SF} in 10 mM potassium phosphate buffer (pH 6.3), 0.2% (w/v) NaN_3, and 5% (v/v) D_2O. For ^{15}N-filtered spectra and dynamical investigations, a sample of uniformly labeled [^{15}N]BMPR-IA_{SF} was used with the protein concentration increased to 1.1 mM for a better signal-to-noise ratio. All spectra were recorded at 298 K on Bruker

DMX600, DMX750, and Avance I 900 spectrometers. Backbone sequential assignments were completed using standard triple-resonance experiments and using selective proton flipback techniques for fast pulsing (*17*). This allowed for the assignment of 91 of 94 non-proline residues in the $^{1}H-^{15}N$ HSQC spectrum. Aliphatic side chain assignments were obtained using a combination of HCCH-TOCSY, CCH-TOCSY, and CCH-COSY experiments, while aromatic assignments were made by linking aromatic spin systems to the respective $C^{\beta}H_2$ protons in a HCH-NOESY spectrum. In summary, resonance assignment was complete for 92 of 102 residues, while for the 10 remaining residues, partial assignments could be made.

To identify the χ_1 rotamer, the prochiral $C^{\beta}H_2$ protons were stereospecifically assigned for 27 of 65 residues. Assignments of χ_1 rotamers were also available for five of seven isoleucine residues and all eight threonine residues. The χ_2 rotamers were assigned for five of seven isoleucine residues and five of seven leucine residues from analysis of intraresidue NOE patterns, leading to stereospecific assignments of the prochiral leucine $C^{\delta}H_3$ groups.

Distance data were derived from a set of four three-dimensional (3D) NOESY spectra, including the heteronuclear-edited NNH- and CNH-NOESY spectra (*18*). In addition to conventional ^{15}N and ^{13}C HSQC-NOESY spectra, a 2D NOESY spectrum was recorded using an unlabeled sample. NOESY cross-peaks were converted into distance ranges by classifying the NOE intensities into four classes, strong, medium, weak, and very weak, resulting in restraints with upper distance boundaries of 2.7, 3.2, 4.0, and 5.0 Å, respectively. For very weak or absent sequential H^N-H^N cross-peaks, a lower distance boundary of 3.2 Å was employed, and for medium-intensity or weaker sequential and intraresidue H^N-H^{α} cross-peaks, a lower distance boundary of 2.7 Å was employed. Additional corrections of the upper limit boundaries were made for pseudoatoms (using r^{-6} averaging) of methyl groups and non-stereospecifically assigned methylene groups. Dihedral angle restraints were derived for backbone ϕ and ψ angles based on C^{α}, C^{β}, C′, and H^{α} chemical shifts using TALOS (*19*). Direct coupling constant restraints were included for the backbone ϕ torsion angles of 60 residues based on $^{3}J_{HNH\alpha}$ coupling constants obtained from an HNHA experiment. Hydrogen bond restraints were applied for 22 residues in secondary structure elements, which showed low water exchange rates, as judged from a MEXICO experiment (*20*). The restraints were applied via inclusion of pseudocovalent bonds as described by Truffault et al. (*21*).

Structure calculation was performed using XPLOR (NIH version 2.9.4). Structures were calculated employing a simulated annealing protocol and refined by a second simulation employing a protocol with two slow cooling stages, the first including a conformational database potential and the second with the force constant for peptide bond planarity relaxed to 50 kcal mol^{-1} rad^{-2}. For the final coordinate ensemble, 50 structures were calculated, of which 20 were chosen on the basis of lowest restraint violations. An average structure was calculated and regularized to give a structure representative of the ensemble (used for figures). Structures were validated with PROCHECK (*22*), WHATCHECK (*23*), and MOLPROBITY (*24*). Refinement was carried out by semiquantitative comparison of experimental and back-calculated ^{15}N HSQC-NOESY, CNH-NOESY, and NNH-NOESY spectra. This process resulted in adjustment of side chain rotamers for several residues. Structure coordinates were deposited in the Protein Data Bank as entry 2k3g.

To obtain data for the backbone dynamics, ^{15}N relaxation measurements (R_1, R_2, and $^{15}N\{^{1}H\}$ heteronuclear NOE) were performed at 298 K and 600 MHz (14.1 T). Twelve different mixing times were recorded for the R_1 and R_2 experiments. Relaxation rates were fitted to peak intensities using software written in house. An initial description of the molecular rotational diffusion tensor was obtained from analysis of R_2/R_1 ratios of individual residues using R2R1_TM and QUADRIC_DIFFUSION (A. G. Palmer, Columbia University, New York, NY) and PDB entry 2k3g. Highly mobile residues or residues with relaxation contributions from chemical exchange were excluded from this estimation. Model-free analysis of the relaxation data of BMPR-IA_{SF} was performed using Modelfree 4.1 (A. G. Palmer) and Fast-Modelfree (*25*−*28*).

RESULTS

Solution Structure of BMPR-IA_{SF}. From crystal structure analysis of BMPR-IA_{ECD} in complex with BMP-2, it is known that the extracellular domain of BMP type I receptor BMPR-IA is structurally distinct from that of type II receptors. Although both BMP receptor subtypes share a common fold that is similar to the three-finger toxins (*29*), structures of type I and type II receptors differ to a large extent. In the type II receptors, the three fingers are formed by three antiparallel two-stranded β-sheets $\beta1\beta2$, $\beta3\beta4$, and $\beta5\beta6$ (*30*). Type I receptor BMPR-IA in its bound conformation, however, does not have a third finger similar to ActR-II (PDB entry 1BTE) since it lacks β-strand 6. In addition, strands $\beta1-\beta5$ are shorter as in ActR-II. The 3_{10}-helix present in the $\beta1\beta2$ loop of ActR-II is absent in BMPR-IA. The $\beta2\beta3$ loop of ActR-II, which is involved in ligand recognition and binding, is seven residues shorter in BMPR-IA. The largest difference, however, is the presence of a 1.6-turn α-helix in BMPR-IA (in its bound conformation) in the region, which corresponds to the $\beta4\beta5$ loop of ActR-II. The formation of this α-helix in BMPR-IA results in a shorter loop length despite the fact that this segment comprises a similar number of residues in BMPR-IA and ActR-II. As a consequence, β-strand 5 of BMPR-IA is equivalent to β-strand 6 of ActR-II, and the α-helix in BMPR-IA is located in front of the central three-stranded β-sheet.

Due to the lack of hydrophobic contacts between residues of the α-helix and the β-sheet we speculated that the helix might not be stable in free BMPR-IA. A preliminary NMR study indeed suggested that the α-helix is disordered in the free conformation; however, no details of the degree of disorder or flexibility were provided (*12*). Our high-resolution NMR structure of BMPR-IA_{SF} now reveals that the loop between β-strands 4 and 5, which contains the α-helix in the bound form, is largely disordered in the free state (Figure 1). The β-strands forming the structural core are well-defined in the unbound conformation and thus form the rigid backbone of BMPR-IA. Except for the $\beta4\beta5$ loop, all loops exhibit rather small root-mean-square deviations (rmsd's) in the unbound conformation. The N-terminus (up to residue

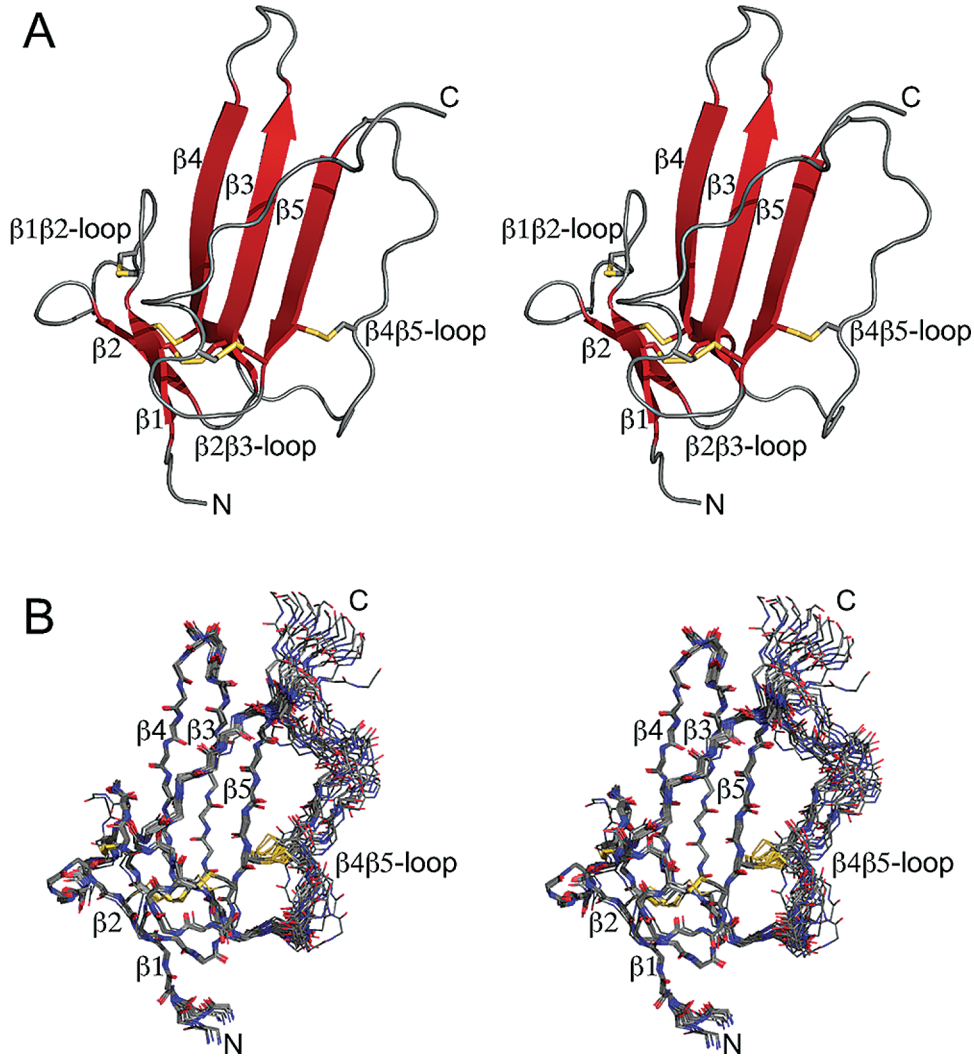

FIGURE 1: Stereoview of the NMR solution structure of BMPR-IA$_{SF}$ in its unbound form. (A) Structure of BMPR-IA$_{SF}$ shown in cartoon representation to highlight secondary structure elements. Two antiparallel β-sheets are formed representing finger 1 and finger 2 in the three-finger toxin fold. (B) Superimposition of the 20 lowest-energy structures obtained from simulated annealing calculations after refinement. The BMPR-IA$_{SF}$ structure ensemble is shown as a main chain stick representation. Disulfide bridges are colored yellow.

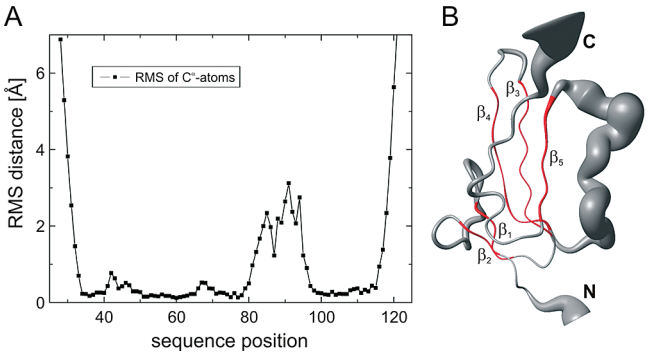

FIGURE 2: (A) Sequence plot of the rmsd of C$^{\alpha}$ atoms within the final structure ensemble shown in Figure 1. The rmsd's are the largest for the N- and C-termini as well as for the $\beta 4\beta 5$ loop. (B) The rms deviation is mapped onto the solution structure of BMPR-IA$_{SF}$, where the diameter is proportional to the rmsd of C$^{\alpha}$ atoms.

Asp31) and the C-terminus (from residue Val118) seem flexible and are disordered in the NMR ensemble (Figures 1 and 2).

The secondary structure elements (except for the missing helix α1) are well established and are stabilized by multiple hydrophobic interactions and a network of 22 main chain−main chain hydrogen bonds. In addition, five disulfide bonds also contribute significantly to the rigid structure, since they connect the loops as well as the N- and C-terminal ends of several β-strands, thereby limiting the conformational flexibility of those loops and strands. Interestingly, the C-terminal loop comprising residues Leu111−Pro117 is highly defined in solution, although it is not part of the regular β-sheet. This might be explained by the "amphipathic" nature of this loop; hydrophobic residues Leu111, Pro113, Leu115, and Pro116 pack against the hydrophobic surface of the central three-stranded β-sheet, formed by residues Ala61, Ile63, and Leu73. The rigid backbone of the β-sheets of fingers 1 and 2 (β-sheets $\beta 1\beta 2$ and $\beta 3\beta 4\beta 5$) is also exemplified by the very small rmsd for the secondary structure elements within the ensemble (0.19 ± 0.07 Å for the backbone and 0.46 ± 0.11 Å for heavy atoms).

Comparison of the Structures of Free and Bound BMPR-IA. The structures of free BMPR-IA$_{SF}$ and BMPR-IA bound to BMP-2 (PDB entry 1REW) are highly similar, showing an average rmsd of 1.35 Å for the β-sheets and connecting loops except for the $\beta 1\beta 2$ and $\beta 4\beta 5$ loops (Figure 3). Significant structural differences are confined to these loop regions. The $\beta 1\beta 2$ loop shows small conformational differ-

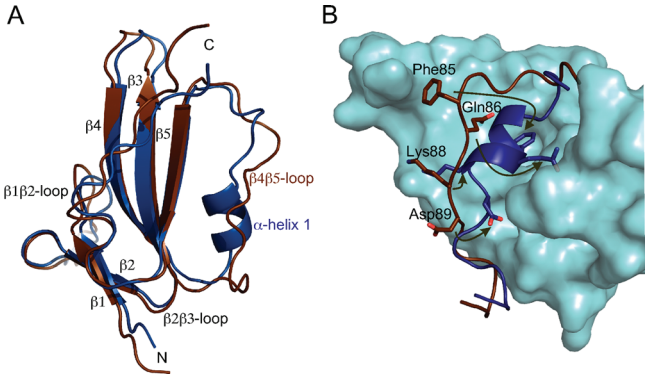

FIGURE 3: Structure comparison of free and bound BMPR-IA. (A) Cartoon representation of the NMR structure of free BMPR-IA$_{SF}$ (red) and BMPR-IA in the binary complex with BMP-2 (PDB entry 1REW) (blue). The core of both receptors represented by the three-stranded β-sheet is highly similar, but clear differences are visible for single loops connecting the β-strands. The $\beta4\beta5$ loop harbors a 1.6-turn helix in bound BMPR-IA which is missing in the free state. (B) Structural changes in the $\beta4\beta5$ loops of free and bound BMPR-IA. BMPR-IA bound to the ligand BMP-2 (cyan surface) is superimposed with free BMPR-IA. Only the $\beta4\beta5$ loops of free (red) and bound (blue) BMPR-IA are shown as backbone trace. Single residues are represented as sticks. The significance of the rearrangement of the $\beta4\beta5$ loop is illustrated by the shifts of Phe85 and Gln86 of BMPR-IA into binding-competent positions. Gln86 represents the main binding determinant in the BMP-2−BMPR-IA interaction, demonstrating that a stable complex can be formed only if the $\beta4\beta5$ loop adopts a helical structure.

ences between the free and bound state with the largest variations for residues Ser41, Gly42, and His43 (C^α atom distances between 2.5 and 3.9 Å). In complex with BMP-2, the $\beta1\beta2$ loop of BMPR-IA contacts the prehelix loop of BMP-2. Therefore, conformational changes in the $\beta1\beta2$ loop might represent a local induced fit to adapt the receptor epitope to the ligand. This observation is of great interest since previous reports suggested that the $\beta1\beta2$ loop is relevant for generating ligand specificity toward different BMP ligands (*31*). GDF-5, another member of the BMP subfamily, specifically binds BMPR-IB, exhibiting a 15-fold lower affinity for BMPR-IA than for BMPR-IB. Sequence comparison of BMPR-IA and BMPR-IB shows that in BMPR-IB Ser41 and Gly42 in the $\beta1\beta2$ loop are replaced with histidines. Introducing substitutions S41H and G42H into BMPR-IA alters the binding properties to GDF-5, thereby underlining the importance of the $\beta1\beta2$ loop for BMP ligand−receptor recognition (*9*). However, since NMR analysis shows that the $\beta1\beta2$ loop is flexible, it remains to be determined whether the loop can indeed adopt different conformations in the context of a different ligand other than BMP-2.

The most evident structural difference between free and bound BMPR-IA is, however, the absence of the 1.6-turn α-helix located in the $\beta4\beta5$ loop of bound BMPR-IA (Figure 3). While in the binary and ternary ligand−receptor complexes of BMP-2 the α-helices of BMPR-IA comprising residues Gly83−Lys88 are identical with respect to backbone and side chain conformations, this helix is completely absent in the structure of the free receptor. In addition, the $\beta4\beta5$ loop is highly disordered (Figure 2), showing large structural variations with distances between corresponding C^α positions of up to 10 Å (Phe85). The residue showing the smallest conformational difference between the free and bound state is Cys87, which is locally fixed by a disulfide bond to Cys101

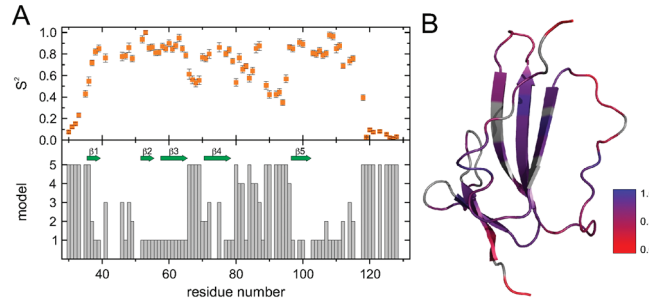

FIGURE 4: (A) Sequence plot of the squared order parameter $\langle S^2 \rangle$ for BMPR-IA$_{SF}$ (top). Model selection for model-free analysis of experimental relaxation data (bottom). (B) $\langle S^2 \rangle$ values mapped onto the solution structure of BMPR-IA$_{SF}$ according to the color bar. Gray residues could not be analyzed.

in β-strand 5. This disulfide bond is located at the C-terminal end of helix α1 in bound BMPR-IA, suggesting a stabilizing effect on a putative helical conformation in the free state.

The C-terminus of BMPR-IA also differs between the free BMPR-IA and BMPR-IA bound to BMP-2. The differences between the C^α positions of corresponding residues range between 1.5 (Gln112) and 3.0 Å (Pro116); however, similar differences are observed when these C^α positions are compared in the binary complex [PDB entry 1REW (*8*)] and the ternary complex [PDB entries 2H62 and 2H64 (*10*)]. A detailed analysis of the crystal structures suggests that some of the conformational differences in the C-terminus of the NMR and crystal structures might be due to crystal-lattice contacts in the crystal structures.

Dynamical Behavior of BMPR-IA: The β4β5 Loop Exhibits Flexibility on the Picosecond to Nanosecond Time Scale. Although nearly all resonances of the $\beta4\beta5$ loop are visible in the $^{15}N-^{1}H$ HSQC spectrum, only short-range NOE contacts (e.g., $H^N_i-H^\alpha$ or $H^N_i-H^\alpha_{i-1}$) but no long-range NOEs were visible. This indicates that a fast motional component is dominant in this region and more than overcompensates for a slow dynamical component. To further elucidate and quantify the background of this observation, we investigated the dynamical behavior of BMPR-IA$_{SF}$ on the picosecond to nanosecond time scale.

Squared order parameters representing the degree of spatial restriction of slow motions could be extracted for 77 residues of BMPR-IA$_{SF}$ using the model-free approach of Palmer et al. (Figure 4) (*26, 27*). Motions within the secondary structure elements of BMPR-IA$_{SF}$ are largely restricted, showing an average squared generalized order parameter $\langle S^2 \rangle$ of 0.84 ± 0.02 ($\langle S^2 \rangle = 0$ presents isotropic disorder, whereas $\langle S^2 \rangle = 1$ presents a fixed orientation). Quantitatively, the average $\langle S^2 \rangle$ of 0.84 corresponds to a semicone angle θ of 19.5 ± 1.1° for the backbone amide bond vector if the "wobbling-in-a-cone" model describing slow internal motions is assumed (*32, 33*). Furthermore, almost all residues within secondary structure elements could be fitted with model 1, which includes only the order parameter as a single fitting parameter (Figure 4). Only in strand $\beta4$ do a few residues exhibit an exchange contribution (model 3 in Figure 4) indicating that these residues have motions on time scales slower than the picosecond time scale characterized by order parameter S^2. Residues of high flexibility on the picosecond to nanosecond time scale are located in loop regions or at the C- or N-terminal end of the protein chain. The region with the smallest order parameters apart from those of the C- and

N-termini is located between strands $\beta4$ and $\beta5$, where nearly all residues are assigned to model 5 (comprising parameters S_f^2, S^2, and $\tau_e = \tau_s$) (Figure 4). In addition, the short $\beta3\beta4$ loop also exhibits an increased flexibility according to NMR relaxation analysis, though less pronounced than that for the $\beta4\beta5$ loop. Usage of model 5 as a fitting model indicates two distinct motional modes: one on the picosecond time scale corresponding to fast librations of the H−N bond vector and a second mode on the nanosecond time scale corresponding to dihedral transitions. Hence, both loops seem to feature a complex motional behavior.

Fast motions within the $\beta3\beta4$ and $\beta4\beta5$ loops are rather restricted and adopt order parameter values similar to those for the secondary structure elements, with an $\langle S^2 \rangle$ of 0.76 ± 0.01 and an $\langle S^2 \rangle$ of 0.73 ± 0.02 for the $\beta3\beta4$ and $\beta4\beta5$ loops, respectively. Consequently, their semicone angles are also similar (24.9 ± 1.1° and 26.7 ± 1.0°, respectively) if a "two-site-jump" model is assumed (*34*), suggesting that the protein transforms quickly between two conformational states. However, inspection of the contribution of the slower motion for these loops to the overall dynamics reveals a significant increase in the semicone angles for amino acids Asp89−Gln94 ($\beta4\beta5$ loop) but only a moderate increase for residues Asp66−Gly69 ($\beta3\beta4$ loop). While in the $\beta4\beta5$ loop semicone angles of up to 54.4° are observed, slower motions in the $\beta3\beta4$ loop are much more restricted, with a maximum semicone angle of 37.3°. The elevated dynamics of the two loops is accompanied by an increase in the water exchange rates (Figure 3 of the Supporting Information).

A very interesting observation is the "stiffening" of residues Gln86 and Cys87. Both residues exhibit a significantly increased squared order parameter (0.76 and 0.81, respectively) and correspondingly a decreased semicone angle. Taking into account the temperature coefficients and the conspicuously decreased water exchange rates of the two residues (Figure 3 of the Supporting Information), participation in a hydrogen bond can be suggested, but at least both residues appear to be protected from the solvent. In addition, both residues were fitted using a model including an exchange contribution (models 3 and 4, respectively, in Figure 4). An exchange contribution, especially for residue Cys87, is supported further by the observation that both residues exhibit increased line widths.

Helix α1 Exists in Nascent Form. A central question raised from the observations was whether helix α1 in the $\beta4\beta5$ loop, though not observed in solution in the ligand-free state, might exist in a nascent form. We thus inspected the carbon chemical shifts and $^3J_{HNHA}$ coupling constants for the corresponding residues (Ser83−Lys88, shaded gray in Figure 5). While sequence plots for C^α and C^β chemical shifts indicate a random coil structure, the C′ chemical shifts suggest an extended, sheetlike structure. On the other hand, analysis of the H^α chemical shifts indicates a shift from random coil structures toward a helical secondary structure. The H^α chemical shifts in this region deviate on average by −0.31 ± 0.15 ppm from values typical for random coil with a deviation larger than ±0.1 ppm considered significant. The discrepancy between C′ and H^α chemical shifts is also observed in the TALOS predictions that are scattered widely across the allowed regions of the Ramachandran plot (Figures 4 and 5 of the Supporting Information). Hence, we cannot deduce a clear trend from TALOS predictions. Therefore,

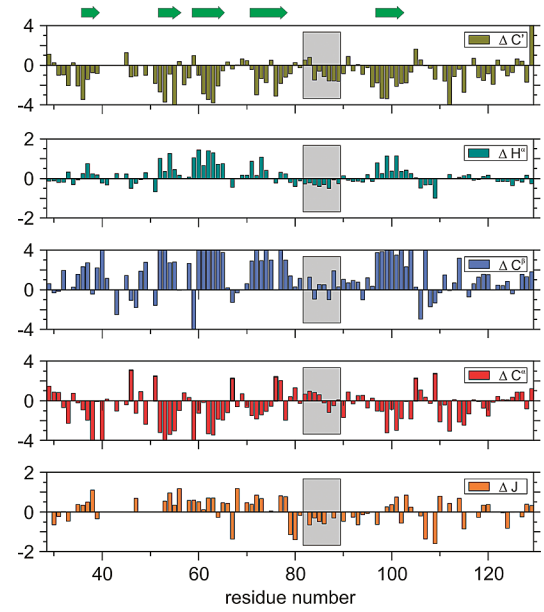

FIGURE 5: Sequence plot of secondary structure indicators for BMPR-IA$_{SF}$. Shown are the chemical shift differences between experimental and random coil chemical shifts for C′, H^α, C^β, and C^α atoms. In addition, the deviation of $^3J_{H^N H^\alpha}$ couplings from the random coil value (6 Hz) is given. Secondary structure elements are indicated at the top.

additionally $^3J_{HNHA}$ coupling constants were investigated, which are systematically lower than values expected for random coil structures, indicating a bias for a helical structure. Thus, in summary, there seems to be a minor preference for a helical structure in the $\beta4\beta5$ loop.

To validate this hypothesis and to clarify whether the α-helix readily forms upon small changes in the environment, we subjected BMPR-IA$_{SF}$ to a titration with increasing concentrations of trifluoroethanol (TFE). TFE is known to induce helix formation on peptides and proteins having an existing helix propensity (*35*). Three regions in BMPR-IA show larger changes upon TFE addition, namely, the N- and C-termini and the $\beta4\beta5$ loop. While in the N-terminal part of the protein the chemical shift changes are very likely to originate from a conformational change in the hydrogen bond between H^N of Leu36 and C′ of Thr55, the changes in the C-terminal part of the protein appear to be more complex. The C-terminal part of the protein adopts a stable conformation, packing against the hydrophobic surface of the central three-stranded β-sheet, but has no regular secondary structure. Thus, the changes in chemical shift seen for the C-terminus likely originate from changes in the extended structure of this segment. In the $\beta4\beta5$ loop, two hot spots, Cys87 and Lys88, exhibit chemical shifts changes larger than 100 ppb upon addition of 10% (v/v) TFE (Figure 6). Other residues such as Ser83, Phe85, and Asp89 show smaller but still significant changes in their H^N chemical shifts. Due to peak overlap, the changes of residue Gln86 representing one of the main determinants of binding of BMPR-IA to BMP-2 could not be evaluated. Since all residues in the helix-forming segment of the $\beta4\beta5$ loop exhibit changes in their chemical shifts upon titration with TFE, a tendency toward helical structure is likely, suggesting that the helix exists in a nascent form.

Thermodynamical Analysis of the Binding of BMPR-IA to BMP-2. We performed isothermal titration calorimetry (ITC)

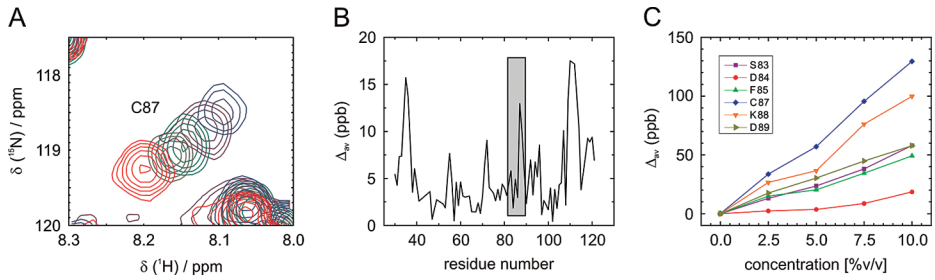

FIGURE 6: Titration studies with TFE on BMPR-IA$_{SF}$. (A) Residue Cys87 exhibits the strongest effects in the $^{1}H-^{15}N$ HSQC spectrum and is shown as an illustrative example. (B) Plot of the average chemical shift $\{\Delta_{av} = [(\Delta\delta_{HN}^2 + \Delta\delta_N^2/5)/2]^{1/2}\}$ plotted vs sequence position. Changes in the chemical shift have been normalized to 1% (v/v) TFE to illustrate the average effect with the increase in TFE concentration. (C) Changes of the average chemical shift (calculated as in Figure 6B) for residues located in the former helix α1 upon titration with increasing amounts of TFE.

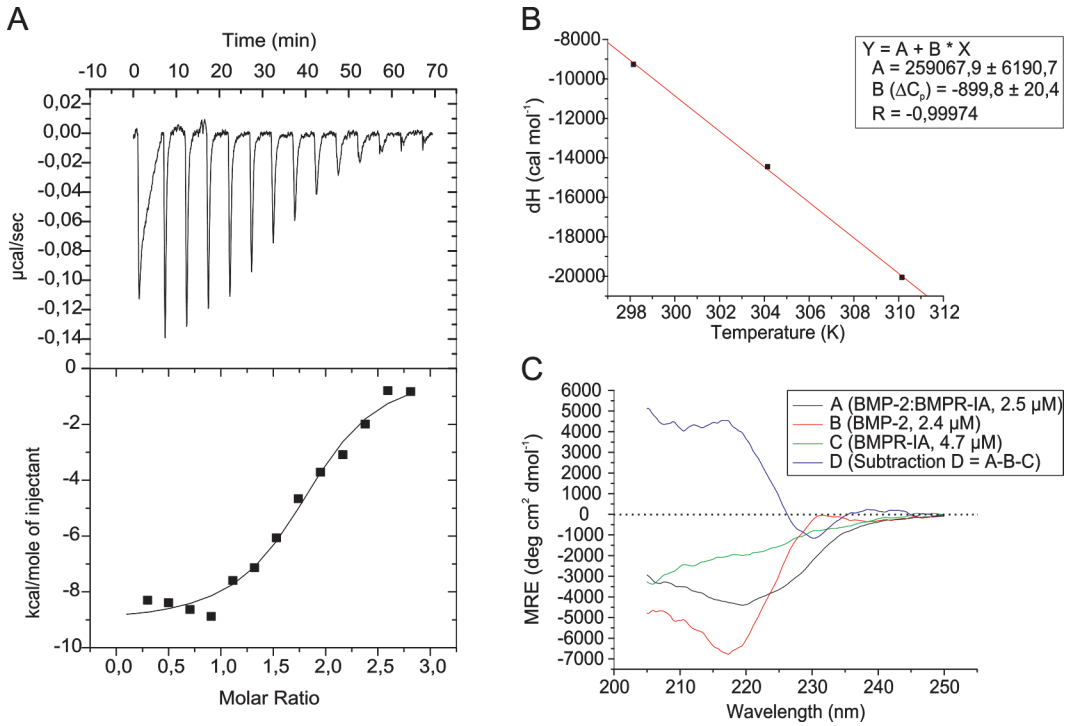

FIGURE 7: (A) Isothermal titration calorimetry of BMP-2 and BMPR-IA. The titration curve obtained after subtracting a reference titration of BMPR-IA into buffer without protein is shown at the top. The integration of the peaks followed by regression analysis gives a sigmoidal curve (bottom). Values for the reaction enthalpy, reaction entropy, stoichiometry of interaction, and binding affinity are summarized in Table 2. (B) The experiment in panel A was repeated at 25, 31, and 37 °C, and the change in enthalpy was plotted vs temperature. The slope of the linear regression line gives the value for the heat capacity (ΔC_p) for formation of the BMP-2−BMPR-IA complex. (C) Circular dichroism spectroscopy of stoichiometric amounts of BMP-2, BMPR-IA, and the BMP-2−BMPR-IA complex dissolved in HBS$_{500}$ buffer which was also used for ITC. Subtracting the spectra obtained for BMP-2 and BMPR-IA from the BMP-2−BMPR-IA complex spectrum results in a strong signal at wavelengths indicative of α-helical structure (~218 nm). A baseline would be expected if there were no structural rearrangements upon binding.

to measure enthalpy and entropy changes upon ligand−receptor interaction to investigate the "disorder-to-order" transition in BMPR-IA (Table 2 and Figure 7). The interaction of BMP-2 with the extracellular domain of BMPR-IA is dominated by an enthalpy release of −9.2 kcal mol^{-1}. The large enthalpy contribution can be explained by taking into account the large number of hydrogen bonds (10 per BMPR-IA molecule; therefore, 20 in total for the dimeric BMP-2) observed in the structure of the BMP-2−BMPR-IA complex. The contribution of individual hydrogen bonds to the binding free energy has been analyzed by mutagenesis (*8, 16*). In folding studies, it was shown that formation of a helix from random coil structures is associated with an enthalpy change of approximately −1 kcal mol^{-1} per residue (*36*). In BMPR-IA, the formation of the small helix comprising six residues would result an enthalpy contribution of roughly −12 kcal mol^{-1} for the two BMPR-IA molecules present in the BMP-2−BMPR-IA complex. Combining the known contribution of the hydrogen bonds in the BMP-2−BMPR-IA interaction with this conformational enthalpy, we would expect a larger enthalpic contribution to the binding free energy, as is experimentally measured. However, other enthalpic terms such as the release of water molecules (solvation enthalpy) are not considered and thus likely partially compensate for the interaction enthalpy generated by the association of the complex (*37*).

The entropy change upon ligand−receptor interaction is slightly positive. However, since solvent entropy is considered the main driving force in the formation of protein−protein interactions (*38*), a larger positive contribution is expected due to the large hydrophobic interface involved in the BMP-2−BMPR-IA interaction. The overall entropy experimentally

Table 1: Solution Structure Statistics and Atomic Root-Mean-Square Deviations[a] for BMPR-IA$_{SF}$

(A) Structural Statistics

	SA	$\langle SA \rangle_r$
rmsd from distance restraints[b] (Å)		
all (655)	0.022 ± 0.002	0.021
intraresidue (167)	0.011 ± 0.004	0.016
inter-residue sequential (249)	0.021 ± 0.003	0.020
medium-range (57)	0.039 ± 0.004	0.037
long-range (182)	0.025 ± 0.006	0.023
rmsd from dihedral restraints (deg) (168)	0.194 ± 0.002	0.162
rmsd from *J* coupling restraints (Hz) (60)	0.889 ± 0.042	0.975
H-bond restraints, averages[c] (Å/deg) (22)	2.17 ± 0.13/14.9 ± 5.4	2.18 ± 0.15/15.2 ± 6.6
H-bond restraints, min−max (Å/deg)	1.94−2.44/5.9−26.6	1.91−2.52/2.8−30.8
deviations from ideal covalent geometry		
bonds ($\times 10^{-3}$ Å)	7.42 ± 0.14	7.27
angles (deg)	0.80 ± 0.02	0.78
impropers (deg)	2.72 ± 1.69	1.63
structure quality indicators[d]		
Ramachandran map regions (%)	87.2/100/0	88/100/0
steric clashes >0.4 Å per 1000 residues	0	0

(B) Atomic rmsd (Å)

	SA vs ⟨SA⟩		SA vs ⟨SA⟩	
	backbone	heavy atoms	backbone	heavy atoms
all structured residues	0.32 ± 0.11	0.78 ± 0.11	0.59 ± 0.12	1.05 ± 0.14
secondary structure	0.19 ± 0.07	0.46 ± 0.11	0.40 ± 0.08	0.78 ± 0.07

[a] Structures are labeled as follows: SA, set of 20 final simulated annealing structures; ⟨SA⟩, mean structure calculated by averaging the coordinates of SA structures after fitting over secondary structure elements; $\langle SA \rangle_r$, the structure obtained by regularizing the mean structure under experimental restraints. [b] Numbers in parentheses indicate the number of restraints of each type. [c] Hydrogen bonds were restrained by treating them as pseudocovalent bonds (see Materials and Methods). Deviations are expressed as the average distance/average deviation from linearity for restrained hydrogen bonds. [d] Determined using MolProbity (*24*). Percentages are for residues in favored (98%), allowed (99.8%), and disallowed regions of the Ramachandran map.

Table 2: Isothermal Titration Calorimetry of BMP-2 and BMPR-IA$_{ECD}$

T (K)	molar ratio	K_D (nM)	ΔH (kcal/mol)	ΔS (cal mol^{-1} K^{-1})	ΔG (kcal mol^{-1})
298.15	1.8	131	−9.2 ± 0.3	0.7	−9.4

	T (K)	ΔC_p (cal mol^{-1} K^{-1})	ΔS_{Solv}[b] (cal mol^{-1} K^{-1})	ΔS_{Conf}[c] (cal mol^{-1} K^{-1})	ΔS_{rt}[d] (cal mol^{-1} K^{-1})
theory[e]	298.15	−884.6[a]	226.1	−228.2	−8
experiment	298.15	−899.8 ± 20.4[f]	230.0	−237.3	−8

[a] The heat capacity was calculated using the relationship $\Delta C_p = 0.45\Delta ASA_{apol} - 0.26\Delta ASA_{pol}$, according to refs *40* and *41* using values for the polar (ΔASA_{pol}) and apolar (ΔASA_{apol}) average surface areas of −1752 and −2978 Å^2, respectively (PDB entry 1REW). [b] The entropy of solvation was calculated using the relationship $\Delta S_{solv} = \Delta C_p \ln(T/T^*)$, where T = 298.15 K and T^* = 385 K according to ref *42*. [c] The conformational entropy is given by the relationship $\Delta S = \Delta S_{solv} + \Delta S_{conf} - \Delta S_{rt}$. [d] The change in the rotational and translational degrees of freedom (ΔS_{rt}) was suggested to be close to the cratic entropy of a bimolecular reaction (*39, 43*). [e] Based on the heat capacity calculated from buried surface areas with the equation given in footnote a. [f] Derived by repeating the titration experiment at 25, 31, and 37 °C. Binding partners were dissolved in 10 mM Hepes (pH 7.4) and 500 mM NaCl. BMPR-IA was titrated into a solution of BMP-2. Experimental values from the enthalpy of reaction (ΔH) were plotted vs temperature (T) (Figure 7). Linear regression analysis gave ΔC_p as the slope of the regression line (R = −0.99974; y = 259067.9 − 899.8x).

measured can be dissected into different entropy terms: the solvation entropy S_{solv}, the conformational entropy S_{conf} accounting for the conformational freedom of the backbone, and the cratic entropy S_{rt} that covers the changes in the rotational and translational degrees of freedom upon forming "one species" from two individual molecules.

If the composition and size of the binding epitopes are known, one can deduce the individual contribution terms, S_{solv}, S_{conf}, and S_{rt}, from the overall entropy using semiempirical equations (*39*−*43*). The buried surface area for the two epitopes in the BMP-2−BMPR-IA complex is known from crystal structure analysis and has a size of 4730 Å^2 with a hydrophobic area comprising 2978 Å^2 (63%). This results in a solvent entropy of 226 cal mol^{-1} K^{-1} (Table 2) and leaves a large negative conformational entropy of −228 cal mol^{-1} K^{-1} for the bimolecular reaction, suggesting that a rather large flexible part in the binding epitope is locked during binding. To verify these contributions, we determined the heat capacity change (ΔC_p) experimentally. The large negative heat capacity change of −900 cal mol^{-1} K^{-1} (Figure 7) corresponds very well with the theoretically calculated heat capacity (Table 2). This analysis shows that the association of the BMP-2−BMPR-IA complex is driven by hydrophobic forces and likely includes structural rearrangments in the binding partners. Circular dichroism experiments further confirm this hypothesis. A strong signal at wavelengths indicative of α-helical structure is seen when the spectra of BMP-2 and BMPR-IA are subtracted from a spectrum of the BMP-2−BMPR-IA complex (Figure 7).

DISCUSSION

In this study, we report the high-resolution NMR structure of the extracellular domain of human BMPR-IA. Although structures of BMPR-IA bound to BMP-2 either in binary or in ternary assemblies have been described previously (*6, 8*−*11*),

a high-resolution structural model of unbound BMPR-IA in solution has not been reported. The comparison of BMPR-IA in its free and ligand-bound forms shows that the five central β-strands forming a three-finger toxin-like fold are rigid and are structurally well conserved. In contrast, two loops connecting strands β1 and β2 as well as strands β4 and β5 undergo significant conformational rearrangements upon ligand binding. The β4β5 loop of BMPR-IA switches between two conformations, random coil in the unbound state and a short 1.6-turn helix in the bound state, depending on whether BMPR-IA is bound to its ligand or BMPR-IA is free in solution. Interestingly, the main binding determinants of BMPR-IA, Phe85 and Gln86, for the BMP-2−BMPR-IA interaction are located in this highly flexible region. Interactions between Phe85 and Gln86 of BMPR-IA and residues of BMP-2 can only be established if the helix α1 is present, implying that a substantial part of the binding free energy can be generated only with a large induced fit of the β4β5 loop. This is in contrast to the ligand binding of structurally similar type II receptors such as ActR-II, where only minor conformational rearrangements of two loop sections are observed (*7, 30*). Residues in the flexible β2β3 and β4β5 loops are located at the periphery of the type II receptor binding epitope, possibly influencing ligand specificity; however, the majority of the interface, especially the main binding determinants, is preformed. In contrast, for type I receptor BMPR-IA, a significant part of the binding interface with BMP-2 is disordered prior to ligand binding and thus requires a disorder-to-order transition.

Comparison of BMP-2 in its free and bound state reveals that the type I receptor epitope of BMP-2 (wrist epitope) also undergoes an induced fit upon type I receptor binding (*11*). The prehelix loop in BMP-2 comprising the hot spot of binding shows displacements for the C^{α} atoms of up to 2.5Å, bringing side chain and backbone groups of the ligand into a binding-competent position. Since the prehelix loop in BMP-2, which directly interacts with the unfolded region in BMPR-IA, is flexible as indicated by increased *B*-factors (residues 49−56; free BMP-2, $B_{C^{\alpha}} = 70.8$ Å^2; bound BMP-2, $B_{C^{\alpha}} = 32.1$ Å^2), the binding epitopes of both binding partners fold "on each other".

The large structural rearrangements observed for the BMP type I receptor−BMP interaction correlate nicely with the slow association rate of the BMP-2−BMPR-IA complex, whereas the interaction of the preformed interfaces of BMP-2 and type II indeed exhibits faster association kinetics. The association rate constant for the BMP-2−BMPR-IA interaction ($k_{on} \sim 3.3 \times 10^5$ M^{-1} s^{-1} for immobilized BMPR-IA) is 1 order of magnitude slower than the rate constant for formation of the complex of BMP-2 with its type II receptors BMPR-II, ActR-II, and ActR-IIB [$k_{on} \sim 1.6 \times 10^6$ M^{-1} s^{-1} for immobilized ActR-II (*6*)]. Compared to those of other protein−protein interaction systems such as the IL4−IL4Rα complex [$k_{on} \sim 1.5 \times 10^7$ M^{-1} s^{-1} for immobilized IL4Rα (*44*)] or the Barnase−Barstar interaction [$k_{on} \sim 6 \times 10^8$ M^{-1} s^{-1} (*45*)], the association rate constant for assembly of the BMP-2−BMPR-IA complex is rather slow, even if rate-increasing effects such as electrostatic steering in the IL-4−IL-4Rα and Barnase−Barstar interaction are taken into account. The IL4−IL4Rα association is hardly dependent on ionic strength and is weakened only slightly at elevated salt concentrations of 0.5−1.0 M NaCl ($k_{on} \sim 0.35 \times 10^7$ M^{-1} s^{-1}) (*44*). Salt concentrations of 0.5 M NaCl also reduce the rate of association of the Barnase−Barstar complex by 40-fold ($k_{on} = 1.6 \times 10^7$ M^{-1} s^{-1}), indicating a significant contribution of electrostatic interactions to binding energy (*45*). However, the association rates at high ionic strengths eliminating electrostatic steering effects are still several order of magnitudes faster than for formation of the BMP-2−BMPR-IA complex. No influence of ionic strength on the rate of association of BMP-2 and BMPR-IA can be observed experimentally (J. Nickel, unpublished results), which confirms results obtained from simulations using HyPare (*46*).

Previous studies have shown that a dynamic interface might be necessary to allow for promiscuous BMP ligand−receptor interaction; however, a rigid scaffold for the receptor core structure is also required to maintain activity (*9*). Mutations of single amino acids observed in the disease juvenile polyposis syndrome (*47*) result in unfolding of BMPR-IA, which therefore cannot bind to BMP ligands anymore. Two affected residues, which are located either at the periphery or far from the interface, exert dramatic effects on the folding of BMPR-IA. By mutagenesis, we found that certain amino acid types with defined chemical or steric properties are required at these positions to maintain the native fold of BMPR-IA (*9*). Despite the large degree of flexibility seen in the NMR structure of BMPR-IA, Tyr39 and Thr55 (both of which are mutated in JPS thereby causing BMPR-IA to unfold) are located in rigid regions. Thus, the flexibility of BMPR-IA possibly allowing adaptation to different ligand surfaces is confined to the region of the β4β5 loop. Other regions require a rigid core structure for maintenance of the overall fold of BMPR-IA. The principle of a rigid scaffold harboring the main binding determinants required for ligand binding and flexible peripheral loops that can modulate binding specificity as seen for the BMP type II receptors is different from the BMP type I receptor−BMP-2 interaction. As we have shown, formation of a complex of BMP-2 and BMPR-IA involves and possibly even requires structural rearrangements in the BMPR-IA β4β5 loop and also the BMP-2 prehelix loop, both of which harbor the main binding determinants of this interaction. Whereas high-affinity binding might also be achieved by employing a rigid helix α1, the structural variability possibly allows modulation of BMP-2-type I receptor recognition specificity as reported previously and thus adds to BMP ligand-type I receptor promiscuity (*9*).

ACKNOWLEDGMENT

We thank M. Gottermeier for excellent technical assistance and Werner Schmitz for his support for mass spectrometry analyses.

SUPPORTING INFORMATION AVAILABLE

A comparison of 2D ^{1}H−^{15}N HSQC spectra of BMPR-IA$_{ECD}$ and BMPR-IA$_{SF}$, assignment of peaks in the 2D ^{1}H−^{15}N HSQC spectrum of BMPR-IA$_{SF}$, results of the MEXICO water exchange experiment, and predictions of torsion angles by TALOS. This material is available free of charge via the Internet at http://pubs.acs.org.

REFERENCES

1. Massague, J. (1998) TGF-β signal transduction. *Annu. Rev. Biochem. 67*, 753–791.

2. Hogan, B. L. M. (1996) Bone morphogenetic proteins: Multifunctional regulators of vertebrate development. *Genes Dev. 10*, 1580–1594.
3. Kishigami, S., and Mishina, Y. (2005) BMP signaling and early embryonic patterning. *Cytokine Growth Factor Rev. 16*, 265–278.
4. Chen, D., Zhao, M., and Mundy, G. R. (2004) Bone morphogenetic proteins. *Growth Factors 22*, 233–241.
5. de Caestecker, M. (2004) The transforming growth factor-β superfamily of receptors. *Cytokine Growth Factor Rev. 15*, 1–11.
6. Allendorph, G. P., Vale, W. W., and Choe, S. (2006) Structure of the ternary signaling complex of a TGF-β superfamily member. *Proc. Natl. Acad. Sci. U.S.A. 103*, 7643–7648.
7. Greenwald, J., Groppe, J., Gray, P., Wiater, E., Kwiatkowski, W., Vale, W., and Choe, S. (2003) The BMP7/ActRII extracellular domain complex provides new insights into the cooperative nature of receptor assembly. *Mol. Cell 11*, 605–617.
8. Keller, S., Nickel, J., Zhang, J. L., Sebald, W., and Mueller, T. D. (2004) Molecular recognition of BMP-2 and BMP receptor IA. *Nat. Struct. Mol. Biol. 11*, 481–488.
9. Kotzsch, A., Nickel, J., Seher, A., Heinecke, K., van Geersdaele, L., Herrmann, T., Sebald, W., and Mueller, T. D. (2008) Structure analysis of BMP-2 type I receptor complexes reveals a mechanism of receptor inactivation in juvenile polyposis syndrome. *J. Biol. Chem. 283*, 5876–5887.
10. Weber, D., Kotzsch, A., Nickel, J., Harth, S., Seher, A., Mueller, U., Sebald, W., and Mueller, T. D. (2007) A silent H-bond can be mutationally activated for high-affinity interaction of BMP-2 and activin type IIB receptor. *BMC Struct. Biol.,* 7.
11. Kirsch, T., Sebald, W., and Dreyer, M. K. (2000) Crystal structure of the BMP-2-BRIA ectodomain complex. *Nat. Struct. Biol. 7*, 492–496.
12. Hatta, T., Konishi, H., Katoh, E., Natsume, T., Ueno, N., Kobayashi, Y., and Yamazaki, T. (2000) Identification of the ligand-binding site of the BMP type IA receptor for BMP-4. *Biopolymers 55*, 399–406.
13. Kirsch, T., Nickel, J., and Sebald, W. (2000) Isolation of recombinant BMP receptor IA ectodomain and its 2:1 complex with BMP-2. *FEBS Lett. 468*, 215–219.
14. Ruppert, R., Hoffmann, E., and Sebald, W. (1996) Human bone morphogenetic protein 2 contains a heparin-binding site which modifies its biological activity. *Eur. J. Biochem. 237*, 295–302.
15. Marley, J., Lu, M., and Bracken, C. (2001) A method for efficient isotopic labeling of recombinant proteins. *J. Biomol. NMR 20*, 71–75.
16. Kirsch, T., Nickel, J., and Sebald, W. (2000) BMP-2 antagonists emerge from alterations in the low-affinity binding epitope for receptor BMPR-II. *EMBO J. 19*, 3314–3324.
17. Diercks, T., Daniels, M., and Kaptein, R. (2005) Extended flip-back schemes for sensitivity enhancement in multidimensional HSQC-type out-and-back experiments. *J. Biomol. NMR 33*, 243–259.
18. Diercks, T., Coles, M., and Kessler, H. (1999) An efficient strategy for assignment of cross-peaks in 3D heteronuclear NOESY experiments. *J. Biomol. NMR 15*, 177–180.
19. Cornilescu, G., Delaglio, F., and Bax, A. (1999) Protein backbone angle restraints from searching a database for chemical shift and sequence homology. *J. Biomol. NMR 13*, 289–302.
20. Gemmecker, G., Jahnke, W., and Kessler, H. (1993) Measurement of Fast Proton-Exchange Rates in Isotopically Labeled Compounds. *J. Am. Chem. Soc. 115*, 11620–11621.
21. Truffault, V., Coles, M., Diercks, T., Abelmann, K., Eberhardt, S., Luttgen, H., Bacher, A., and Kessler, H. (2001) The solution structure of the N-terminal domain of riboflavin synthase. *J. Mol. Biol. 309*, 949–960.
22. Laskowski, R. A., Macarthur, M. W., Moss, D. S., and Thornton, J. M. (1993) Procheck: A Program to Check the Stereochemical Quality of Protein Structures. *J. Appl. Crystallogr. 26*, 283–291.
23. Hooft, R. W. W., Vriend, G., Sander, C., and Abola, E. E. (1996) Errors in protein structures. *Nature 381*, 272.
24. Lovell, S. C., Davis, I. W., Adrendall, W. B., de Bakker, P. I. W., Word, J. M., Prisant, M. G., Richardson, J. S., and Richardson, D. C. (2003) Structure validation by Cα geometry: ϕ, ψ and Cβ deviation. *Proteins: Struct., Funct., Genet. 50*, 437–450.
25. Cole, R., and Loria, J. P. (2003) FAST-Modelfree: A program for rapid automated analysis of solution NMR spin-relaxation data. *J. Biomol. NMR 26*, 203–213.
26. Lipari, G., and Szabo, A. (1982) Model-Free Approach to the Interpretation of Nuclear Magnetic-Resonance Relaxation in Macromolecules. 1. Theory and Range of Validity. *J. Am. Chem. Soc. 104*, 4546–4559.
27. Lipari, G., and Szabo, A. (1982) Model-Free Approach to the Interpretation of Nuclear Magnetic-Resonance Relaxation in Macromolecules. 2. Analysis of Experimental Results. *J. Am. Chem. Soc. 104*, 4559–4570.
28. Mandel, A. M., Akke, M., and Palmer, A. G. (1995) Backbone Dynamics of *Escherichia coli* Ribonuclease Hi: Correlations with Structure and Function in an Active Enzyme. *J. Mol. Biol. 246*, 144–163.
29. Rees, B., and Bilwes, A. (1993) Three-dimensional structures of neurotoxins and cardiotoxins. *Chem. Res. Toxicol. 6*, 385–406.
30. Greenwald, J., Fischer, W. H., Vale, W. W., and Choe, S. (1999) Three-finger toxin fold for the extracellular ligand-binding domain of the type II activin receptor serine kinase. *Nat. Struct. Biol. 6*, 18–22.
31. Nickel, J., Kotzsch, A., Sebald, W., and Mueller, T. D. (2005) A single residue of GDF-5 defines binding specificity to BMP receptor IB. *J. Mol. Biol. 349*, 933–947.
32. Lipari, G., and Szabo, A. (1980) Effect of librational motion on fluorescence depolarization and nuclear magnetic resonance relaxation in macromolecules and membranes. *Biophys. J. 30*, 489–506.
33. Lipari, G., and Szabo, A. (1981) Pade Approximants to Correlation-Functions for Restricted Rotational Diffusion. *J. Chem. Phys. 75*, 2971–2976.
34. Clore, G. M., Driscoll, P. C., Wingfield, P. T., and Gronenborn, A. M. (1990) Analysis of the Backbone Dynamics of Interleukin-1-β Using 2-Dimensional Inverse Detected Heteronuclear ^{15}N–^{1}H NMR Spectroscopy. *Biochemistry 29*, 7387–7401.
35. Buck, M. (1998) Trifluoroethanol and colleagues: Cosolvents come of age. Recent studies with peptides and proteins. *Q. Rev. Biophys. 31*, 297–355.
36. Scholtz, J. M., Marqusee, S., Baldwin, R. L., York, E. J., Stewart, J. M., Santoro, M., and Bolen, D. W. (1991) Calorimetric determination of the enthalpy change for the α helix to coil transition of an alanine peptide in water. *Proc. Natl. Acad. Sci. U.S.A. 88*, 2854–2858.
37. Luke, K., Apiyo, D., and Wittung-Stafshede, P. (2005) Dissecting homo-heptamer thermodynamics by isothermal titration calorimetry: Entropy-driven assembly of co-chaperonin protein 10. *Biophys. J. 89*, 3332–3336.
38. Chothia, C., and Janin, J. (1975) Principles of protein-protein recognition. *Nature 256*, 705–708.
39. Lavigne, P., Bagu, J. R., Boyko, R., Willard, L., Holmes, C. F., and Sykes, B. D. (2000) Structure-based thermodynamic analysis of the dissociation of protein phosphatase-1 catalytic subunit and microcystin-LR docked complexes. *Protein Sci. 9*, 252–264.
40. Murphy, K. P., Bhakuni, V., Xie, D., and Freire, E. (1992) Molecular basis of co-operativity in protein folding. III. Structural identification of cooperative folding units and folding intermediates. *J. Mol. Biol. 227*, 293–306.
41. Murphy, K. P., and Freire, E. (1992) Thermodynamics of structural stability and cooperative folding behavior in proteins. *Adv. Protein Chem. 43*, 313–361.
42. Murphy, K. P., Freire, E., and Paterson, Y. (1995) Configurational effects in antibody-antigen interactions studied by microcalorimetry. *Proteins 21*, 83–90.
43. Murphy, K. P., Xie, D., Thompson, K. S., Amzel, L. M., and Freire, E. (1994) Entropy in biological binding processes: Estimation of translational entropy loss. *Proteins 18*, 63–67.
44. Shen, B. J., Hage, T., and Sebald, W. (1996) Global and local determinants for the kinetics of interleukin-4/interleukin-4 receptor α chain interaction: A biosensor study employing recombinant interleukin-4-binding protein. *Eur. J. Biochem. 240*, 252–261.
45. Schreiber, G., and Fersht, A. R. (1993) Interaction of Barnase with Its Polypeptide Inhibitor Barstar Studied by Protein Engineering. *Biochemistry 32*, 5145–5150.
46. Shaul, Y., and Schreiber, G. (2005) Exploring the charge space of protein-protein association: A proteomic study. *Proteins 60*, 341–352.
47. Howe, J. R., Sayed, M. G., Ahmed, A. F., Ringold, J., Larsen-Haidle, J., Merg, A., Mitros, F. A., Vaccaro, C. A., Petersen, G. M., Giardiello, F. M., Tinley, S. T., Aaltonen, L. A., and Lynch, H. T. (2004) The prevalence of MADH4 and BMPR1A mutations in juvenile polyposis and absence of BMPR2, BMPR1B, and ACVR1 mutations. *J. Med. Genet. 41*, 484–491.

BI801059J